Electronic Supplementary Material (ESI) for Sustainable Energy & Fuels.
This journal is © The Royal Society of Chemistry 2018

Supporting Information

Contribution of electrolyte in nanoscale electrolysis of pure and buffered water by particulate photocatalysis

Muhammad Qureshi,[a] Angel T. Garcia-Esparza,[b†] Tatsuya Shinagawa,[a‡] Philippe Sautet,[c,d] Tangui Le Bahers,[b] and Kazuhiro Takanabe[a*]

[a] King Abdullah University of Science and Technology (KAUST), KAUST Catalysis Center (KCC) and Physical Sciences and Engineering Division, 4700 KAUST, Thuwal, 23955-6900, Saudi Arabia.

[b] Univ Lyon, ENS de Lyon, CNRS, Université Claude Bernard Lyon 1, Laboratoire de Chimie UMR 5182, F-69342 Lyon, France.

[c] Department of Chemical and Biomolecular Engineering, University of California Los Angeles (UCLA), Los Angeles, CA 90095, United States.

[d] Department of Chemistry and Biochemistry, University of California Los Angeles, Los Angeles, CA 90095, United States.

[†] Present address: Stanford Synchrotron Radiation Light Source, SLAC National Accelerator Laboratory, Menlo Park, California 94025, United States

[‡] Present address: Department of Chemistry and Applied Biosciences, Institute for Chemical and Bioengineering, ETH Zurich, Vladmir-Prelog-Weg 1, CH-8093 Zurich, Switzerland.

Corresponding author: Kazuhiro Takanabe

e-mail: kazuhiro.takanabe@kaust.edu.sa

Relationship between photocatalytic and electrocatalytic rates

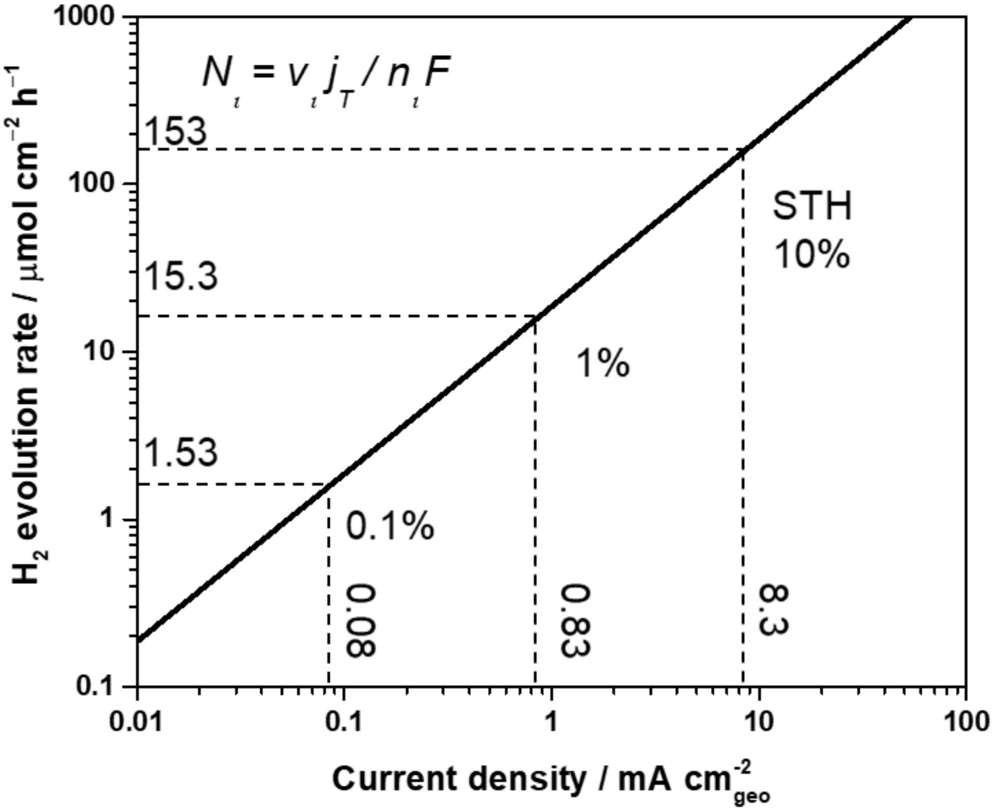

Figure S1. Correlation among H_2 evolution rate, solar-to-hydrogen (STH) energy efficiency and current density (normalized per geometric surface area).

Inhibition of the oxygen reduction reaction by a Cr-based coating

A cyclic voltammogram of a Pt rotating disk electrode (RDE) in 0.5 M K_2SO_4 at pH 6 with oxygen bubbling is shown in Figure S2. At 0.6 V on the reversible hydrogen electrode (RHE) scale, an increasing cathodic current density was observed and reached a constant current density of –5 mA cm^{-2} at approximately 0~0.5 V vs. RHE. The constant current indicates a limitation by mass transport that is ascribable to the oxygen diffusion-limited oxygen reduction reaction (ORR, water-forming reaction).[1] Further increases in the cathodic current below 0 V vs. RHE are assigned to the hydrogen evolution reaction (HER), as we previously reported.[2] The CrO_x/Pt RDE in the same unbuffered electrolyte showed negligible current at –0.3~0.7 V vs. RHE, and an increase in cathodic current below –0.3 V vs. RHE was ascribable to HER. The absence of limiting diffusion currents clearly suggests nearly complete selective suppression of ORR by the CrO_x layer without a significant loss of HER activity of the substrate (Pt), consistent with previous reports.[3] In the buffered electrolyte of K-phosphate, the CrO_x/Pt RDE exhibited a monotonically increasing current density below 0 V vs. RHE. The shift in the onset potential for HER by the introduction of buffered species originates from the prevention of the reduction of water molecules responsible for HER, as we reported elsewhere.[4] Losses due to the crossover of product gases were neglected in our simulations below because the experimental CrO_x/Pt/$SrTiO_3$ system was designed to avoid activating reverse water-forming reactions from H_2 and O_2 products by the use of the CrO_x modifier.

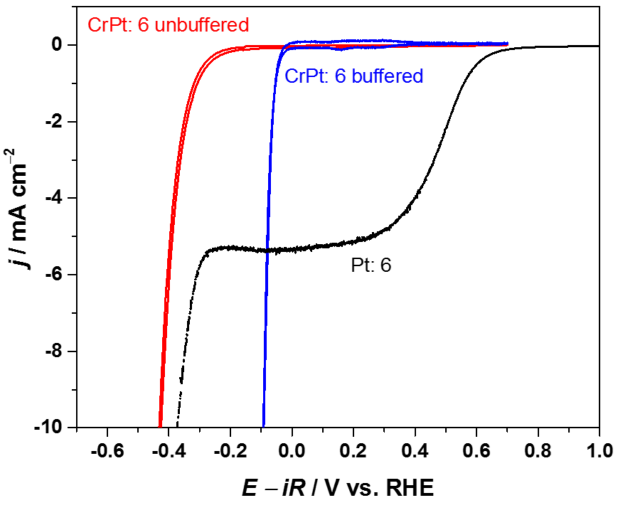

Figure S2. Cyclic voltammograms over a Cr-modified Pt (CrO_x/Pt) RDE in 0.5 M K_2SO_4 at pH 6 and in 0.5 M K-phosphate (KH_2PO_4/K_2HPO_4=80/20, pH 5.8) and a pristine Pt RDE in 0.5 M K_2SO_4 at pH 6 (dotted line) (conditions: 3600 rpm, 50 mV s^{-1}, O_2 bubbling and 298 K).

Optimization of electrocatalyst loading on the semiconductor

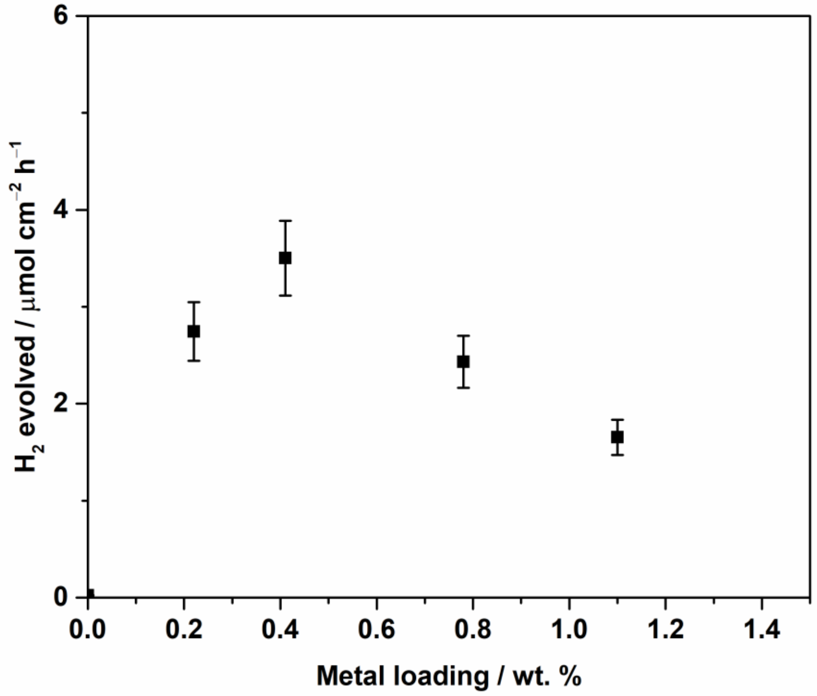

Figure S3. Photocatalytic time course of Pt/SrTiO$_3$ as a function of metal loading in 10% methanol solution (300 < λ < 800 nm, 50 mg of catalyst, 100 mL solution, 38.5 cm^2 irradiated area).

Simulation model

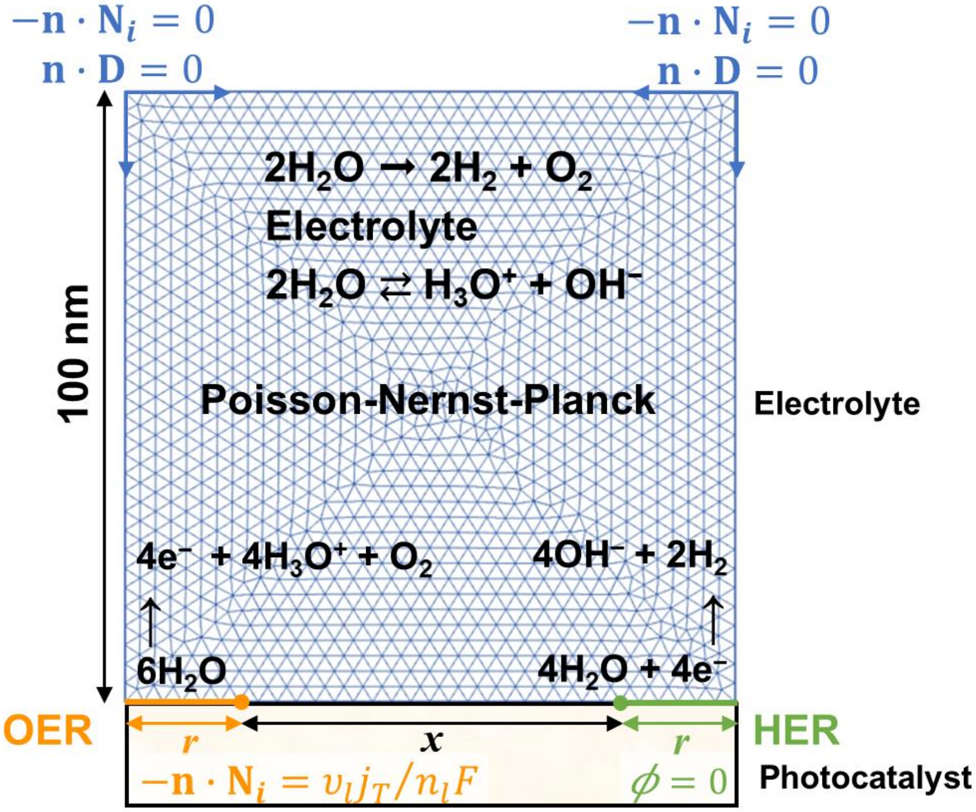

Figure S4. Nanoelectrolysis scheme representing the model of the cross-section of the electrolyte volume at the interface with the redox sites on the surface of a semiconductor photocatalyst (this scheme is not to scale).

The simulations consider 100 nm of electrolyte away from the surface of the semiconductor. The boundaries of size *r* at the bottom of the figure represent the OER and HER sites on the left and right, respectively. The uncertainty of the location of the OER sites was overcome by the arbitrary variation in the inter-particle distance (x) from 5 to 110 nm. On the bottom right side, the HER boundary was treated as ground ($\phi = 0$). Insulating boundary conditions with no flux and no charge were considered on the other walls of the box model. Water-splitting simulations were computed by utilizing triangular mesh elements of equal size, as represented with blue lines in the figure. The figures in the main text represent an extended array of mirror images of the calculated database in the two-dimensional domain in Figure S4. Potential fluctuations and losses arising from the complexity of surface states at the semiconductor-liquid junction were not considered in our model for simplicity (i.e., absorbed potential-determining ions, defects, passivated domains, etc.). Nevertheless, such phenomena may be treated as a secondary phenomenological potential term in future studies.

Table S1

Simulation parameters.

Symbols	Values	Units	Description
x	$5\times10^{-9} - 11\times10^{-8}$	m	Inter-particle distance between redox sites
r	3×10^{-9}	m	Size of the redox site and out-of-plane thickness
r^2	9×10^{-18}	m^2	Surface area
E^0	1.23	V	Standard redox potential
σ_{MilliQ}	5.5×10^{-6}	$\mathrm{S\ m^{-1}}$	Milli-Q water conductivity
$\sigma_{\mathrm{0.5M}}$	1×10^{-1}	$\mathrm{S\ m^{-1}}$	Approximated conductivity of a 0.5 M supporting electrolyte
pH^0	7		Initial pH of the solution
$c^0_{\mathrm{H30+}}$	1×10^{-4}	$\mathrm{mol\ m^{-3}}$	Initial concentration of hydronium ions
$c^0_{\mathrm{OH-}}$	1×10^{-4}	$\mathrm{mol\ m^{-3}}$	Initial concentration of hydroxide ions
$D_{\mathrm{H30+}}$	9.3×10^{-9}	$\mathrm{m^2\ s^{-1}}$	Diffusion coefficient of hydronium ions in water
$D_{\mathrm{OH-}}$	5.3×10^{-9}	$\mathrm{m^2\ s^{-1}}$	Diffusion coefficient of hydroxide ions in water
$z_{\mathrm{OH-}}$	1		Charge of the hydronium ions
$z_{\mathrm{OH-}}$	-1		Charge of the hydroxide ions
K_{eq}	1×10^{-8}		Equilibrium constant
$10^{-a/b}{}_{HER}$	1×10^{-2}	$\mathrm{mA\ cm^{-2}}$	HER Tafel parameter
$10^{-a/b}{}_{OER}$	2×10^{-3}	$\mathrm{mA\ cm^{-2}}$	OER Tafel parameter
b	120	$\mathrm{mV\ dec^{-1}}$	Tafel slope
n	4		Number of electrons
ε_r	80		Relative permittivity
Constants			
T	298	K	Temperature
ε^0	8.8542×10^{-12}	$\mathrm{F\ m^{-1}}$	Vacuum permittivity
F	96485.3	$\mathrm{C\ mol^{-1}}$	Faraday constant
k_B	1.3806×10^{-23}	$\mathrm{J\ K^{-1}}$	Boltzmann constant
e	1.6022×10^{-19}	C	Electron charge
h	6.6261×10^{-34}	J s	Planck's constant
R	8.3145	$\mathrm{J\ mol^{-1}\ K^{-1}}$	Universal constant
RT	2477.7	$\mathrm{J\ mol^{-1}}$	*RT* constant factor
F/RT	38.941	$\mathrm{V^{-1}}$	*f* constant for electrochemical kinetics
m	5×10^{-10}	m	Equilateral mesh element size

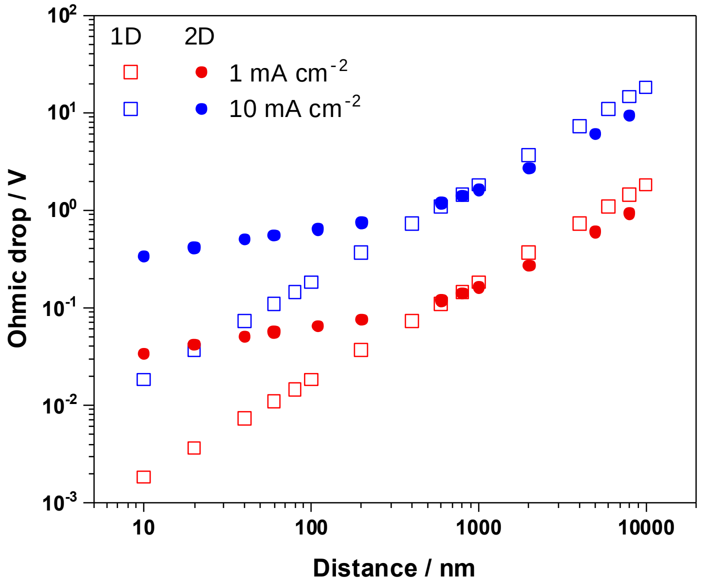

Figure S5. Ohmic drop over 1D and 2D systems as a function of distance between the anode and cathode.

The data shown in Figure S5 captures the cases of longer distance between electrodes using simplified simulations by neglecting mass transport and thus removing the diffusion component in eqn. 2 in the main manuscript. Consequently, the current vector may be described as a function of the potential by assuming electroneutrality $\sum z_i c_i = 0$. It is then possible to define an isotropic conductivity and derive ohmic charge transport in the solution if the concentration gradients are neglected. The conductivity of Milli-Q water was used in our study following its use in the photocatalytic experiments ($\sigma_l = 5.5\times10^{-6}$ S m^{-1}).

$$i = -\frac{F^2}{RT}\nabla\phi\sum z_i^2 D_i c_i = -\sigma_l \nabla\phi \qquad \text{(S1)}$$

Photocatalytic reaction in the presence of an electron accepter or donor

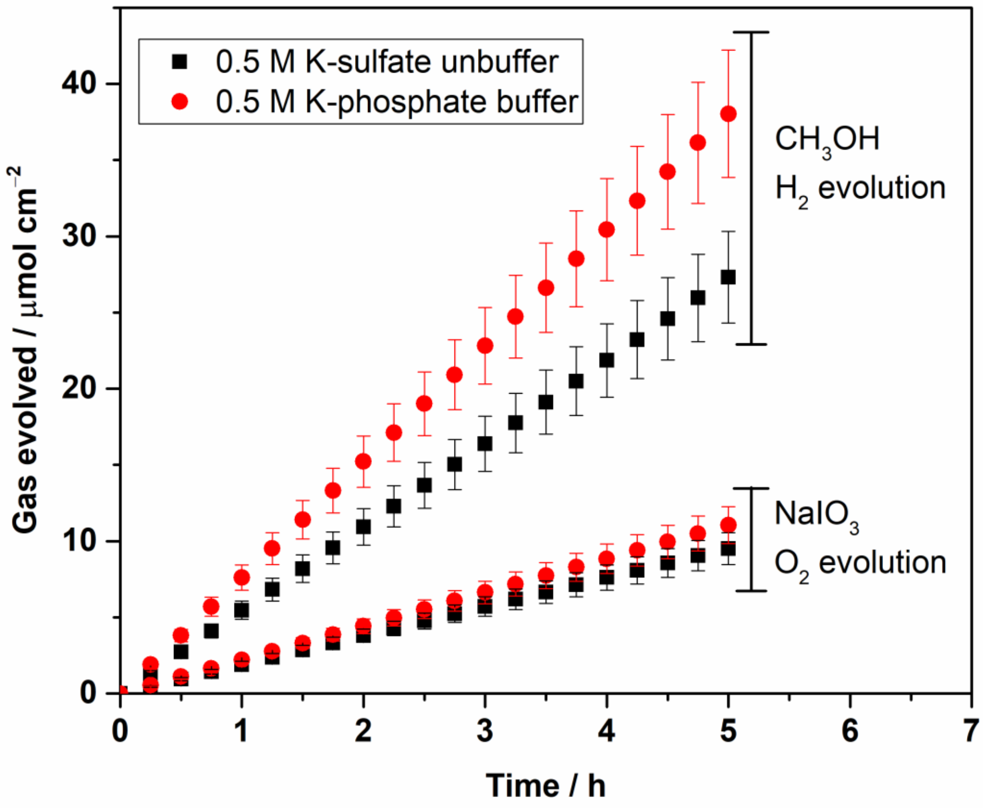

Figure S6. Photocatalytic activity time course for Pt/$SrTiO_3$ with 0.5 M K-sulfate and 0.5 M K-phosphate with either 5% methanol solution or 100 mM iodate solution as a hole or electron scavenger, respectively ($300 < \lambda < 800$ nm, 50 mg of catalyst, 515 mL volume of reactor, 38.5 cm^2 reactor area).

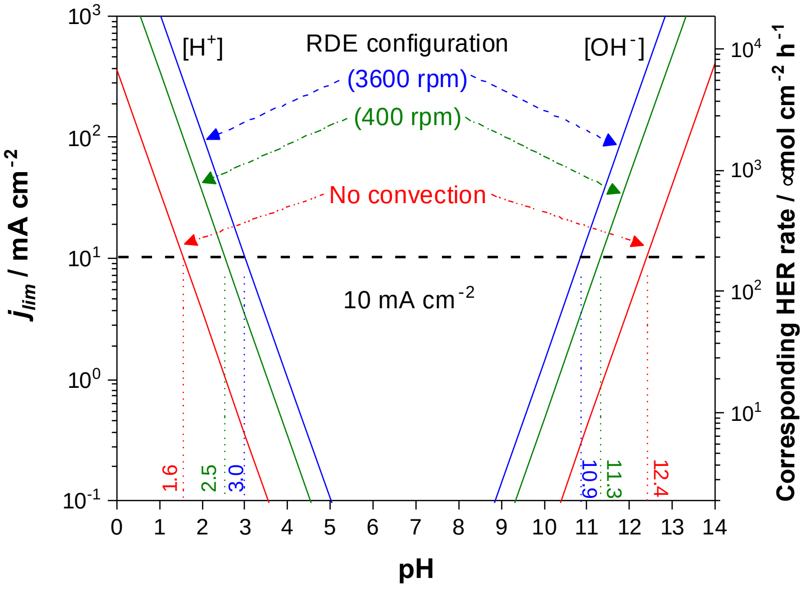

Figure S7. Expected limiting diffusion current density for the reduction of H^+ and oxidation of OH^- on a substrate for rotation speeds of 400 and 3600 rpm as well as with no convection. The corresponding hydrogen evolution rate in overall water splitting is plotted on the second y-axis.

In a conventional supporting electrolyte in the absence of any buffering actions, i.e., unbuffered near-neutral pH conditions, the HER rate over a HER-active electrocatalyst can readily be limited by the diffusion of protons at appreciable current densities due to the small proton activity. For example, at pH 7 (10^{-7} mol L^{-1}), the diffusion flux of protons is merely on the microampere scale (Figure S10). To achieve substantial reaction rates, e.g., 10 mA cm^{-2} (which corresponds to an STH efficiency of ~10%), the water molecule has to act as the reactant for the HER (i.e., reactant switching). Nevertheless, the reduction of the water molecule is kinetically slower than that of protons, and the overall performance is significantly lower due to the kinetic activation loss.

In such circumstances, the introduction of a buffer effectively supplies protons as the HER reactant to the active site (i.e., the buffer functions as a proton carrier), whereby the diffusion limitation, as well as the kinetically slow H_2O reduction, can be circumvented. The apparent improvement in the performance by the introduction of a buffer was significant: while the overpotential required to achieve 10 mA cm^{-2} was ~780 mV in the conventional supporting electrolyte of 0.5 M K_2SO_4 (pH 6), the same current density was readily reached at a overpotential of merely ~420 mV in 0.5 M NaH_2PO_4 over CrO_x/Pt RDE (Figure S8).[5] In brief, this observation indicates that since the buffer species presumably functions as a proton carrier, the performance would be further improved by increasing the concentration of the proton carrier.

We examined the HER on pristine polycrystalline Pt under buffered near-neutral pH conditions in detail in our previous study.[4] We first investigated the influences of the concentration of phosphate at pH 5 on the HER performance, which revealed that in the low-concentration regime, the HER performance indeed improved with an increase in the concentration; however, above a threshold concentration of ~2 mol L^{-1}, the HER performance was reduced in denser electrolytes. As an attempt to rationalize this volcano-shaped relationship between the HER performance and the phosphate concentration, we developed a model accounting for the HER under buffered conditions. The buffered species in the protonated form (e.g., $H_2PO_4^-$) diffuses to the HER active site, where it releases its proton that is consumed for the HER; then, the remaining deprotonated species (e.g., HPO_4^{2-}) diffuses back to the bulk of the electrolyte, where it is protonated via the acid/base equilibrium (e.g., $HPO_4^{2-} + H^+ = H_2PO_4^-$). By our previously reported microkinetic and mass-transport phenomena analysis,[4] the experimental observations were successfully reproduced, and importantly, the major limiting factor was identified: Regardless of the phosphate concentration, the diffusion of the proton carrier to the HER active site, i.e., the buffered species (such as $H_2PO_4^-$ and HCO_3^-), largely limits the HER performance. This finding indicates that the tuning of the electrolyte property to maximize the diffusion flux, i.e., electrolyte engineering, is a powerful concept for improving the HER performance in the buffered near-neutral pH conditions.

We then further examined the HER in various electrolytes on pristine Pt disks, as previously reported elsewhere.[6] The experimentally observed HER performances were indeed well rationalized by addressing the electrolyte properties, which clearly validated our hypothesis. The identified key factors determining the apparent HER performance are (1) the diffusion coefficient of the proton carrier, (2) the activity of the proton carrier, and (3) the thickness of the diffusion layer. These factors can be reduced into primary parameters: (a) the effective ion size in hydrated form, (b) the viscosity of the electrolyte, (c) the mean activity coefficient, and (d) the molarity. According to this rationale, a buffered electrolyte that yields larger fluxes of the proton carrier meets the following criteria: (i) smaller buffered species (proton carrier) in a hydrated form, (ii) lower viscosity, (iii) larger mean activity coefficient at a given molarity, and more specifically less association between cation and anion.

At this point in the discussion, we must state that when the whole series of available buffer species are considered, additional criteria other than diffusion has to be considered in practice, namely, the migration event (or ohmic loss). As an example, let us now consider the typical buffer solutions of carbonate and borate. These electrolytes at near-neutral pH contain the nonionic species of carbonic acid (H_2CO_3) and boric acid (H_3BO_3). Due to the absence of electrostatic interactions of these species with coexisting ions in hydrated form, association of the proton carrier would not occur, which leads to a larger mean activity coefficient and in turn an improved diffusion flux. However, the nonionic nature of these species indicates their negligible contribution to the migration events, which correspondingly enlarges the ohmic drop (*iR* loss), possibly leading to poorer overall performance. One may think that, if these electrolytes are to be employed, additional ionic species can be supplied to improve the ionic conductivity of the system. Unfortunately, however, the coexisting ions significantly complicate the system.[7] In particular, in the dense electrolytes, such as 1.5 mol L^{-1}, the theoretical rationalization is practically impossible even today, and the field of specific ion effects is a significant active research topic currently and beyond the scope of this work. Alternatively, one may think about organic buffer solutions. Unfortunately, organic buffer species are generally larger in size, which thus have smaller diffusion coefficients. Nevertheless, by appropriate engineering of the molecule for half-cell studies employing a membrane, it might be appropriate. However, in the membrane-less overall water-splitting system studied herein, they typically cannot sustainably function as a buffer because the organic species are readily oxidized at the anodic sites. For example, when citrate buffer is employed for the study of the oxygen evolution reaction (OER), the Faradaic efficiency toward O_2 is merely 40%, presumably due to the oxidation of citrate.[8]

In this context, phosphate buffer is the only appropriate choice of buffer for scientific interest. Among the various phosphate buffer solutions at near-neutral pH levels, the reported guidelines predict that the mixture of KH_2PO_4 and K_2HPO_4 would realize the highest diffusion flux and in turn the highest HER performance, which we successfully confirmed experimentally. In the optimal K-phosphate electrolyte, the overpotential required to reach 10 mA cm^{-2} was only 40 mV, which is fairly comparable to that under extremely acidic conditions (~20 mV) over pristine Pt disk electrodes. In the main manuscript, we show and emphasize that these electrochemical studies can be readily transferred to photocatalytic systems. As described in the current study, the highest performance in the K-phosphate solutions was observed at pH ~6, in which both $H_2PO_4^-$ and HPO_4^{2-} coexist, in excellent agreement with the electrochemical system. Consistently, we must stress that additional aspects need to be considered when buffered solutions are used in particulate photocatalytic overall water splitting, including wettability and bubble formation. Most importantly, the dispersivity of the photocatalyst powders in the system is also of major concern for efficient light absorption and calls for further fundamental investigations.

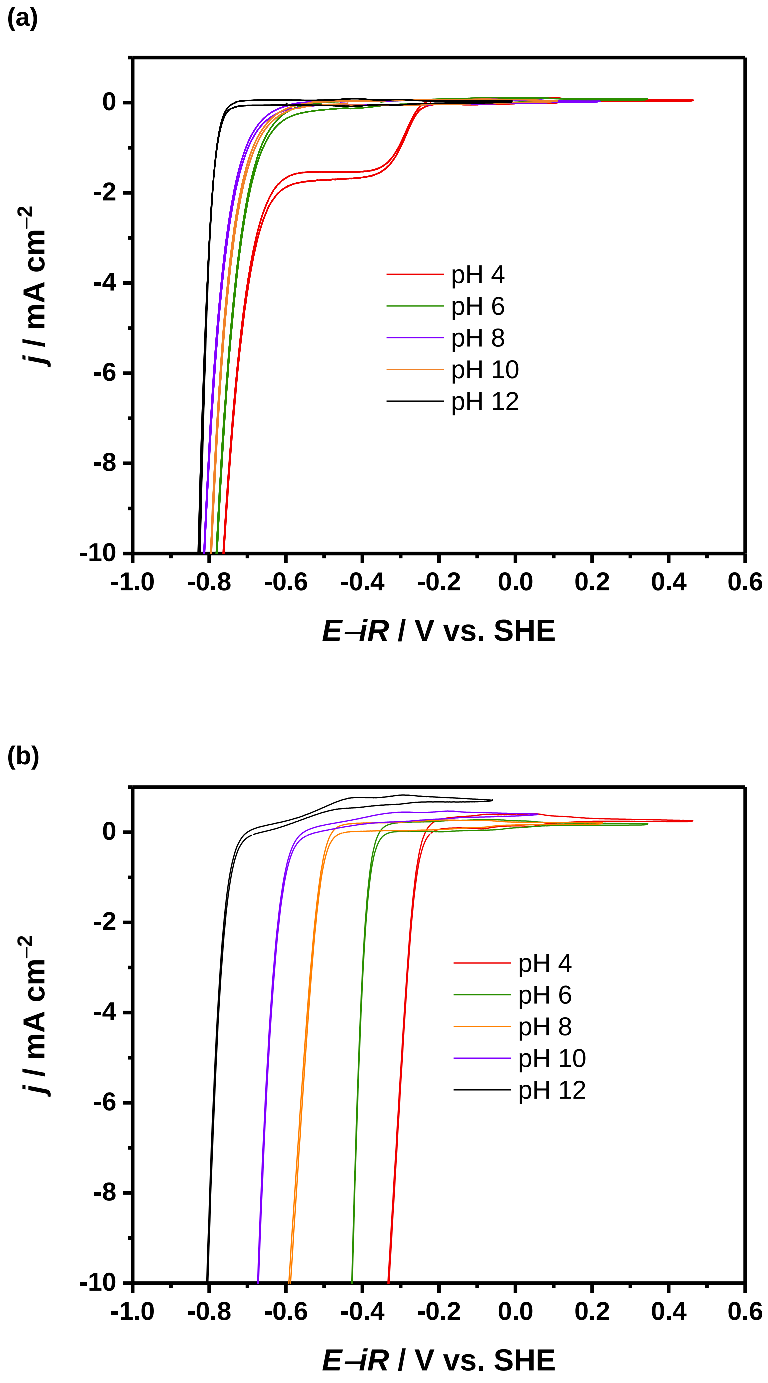

Figure S8. Cyclic voltammograms over a CrO_x/Pt RDE in (a) 0.5 M K_2SO_4 and in (b) 0.5 M phosphate buffer solution at various pH values (conditions: 3600 rpm, 50 mV s^{-1}, H_2 bubbling and 298 K).

UV-Vis diffuse reflectance spectra and photon flux

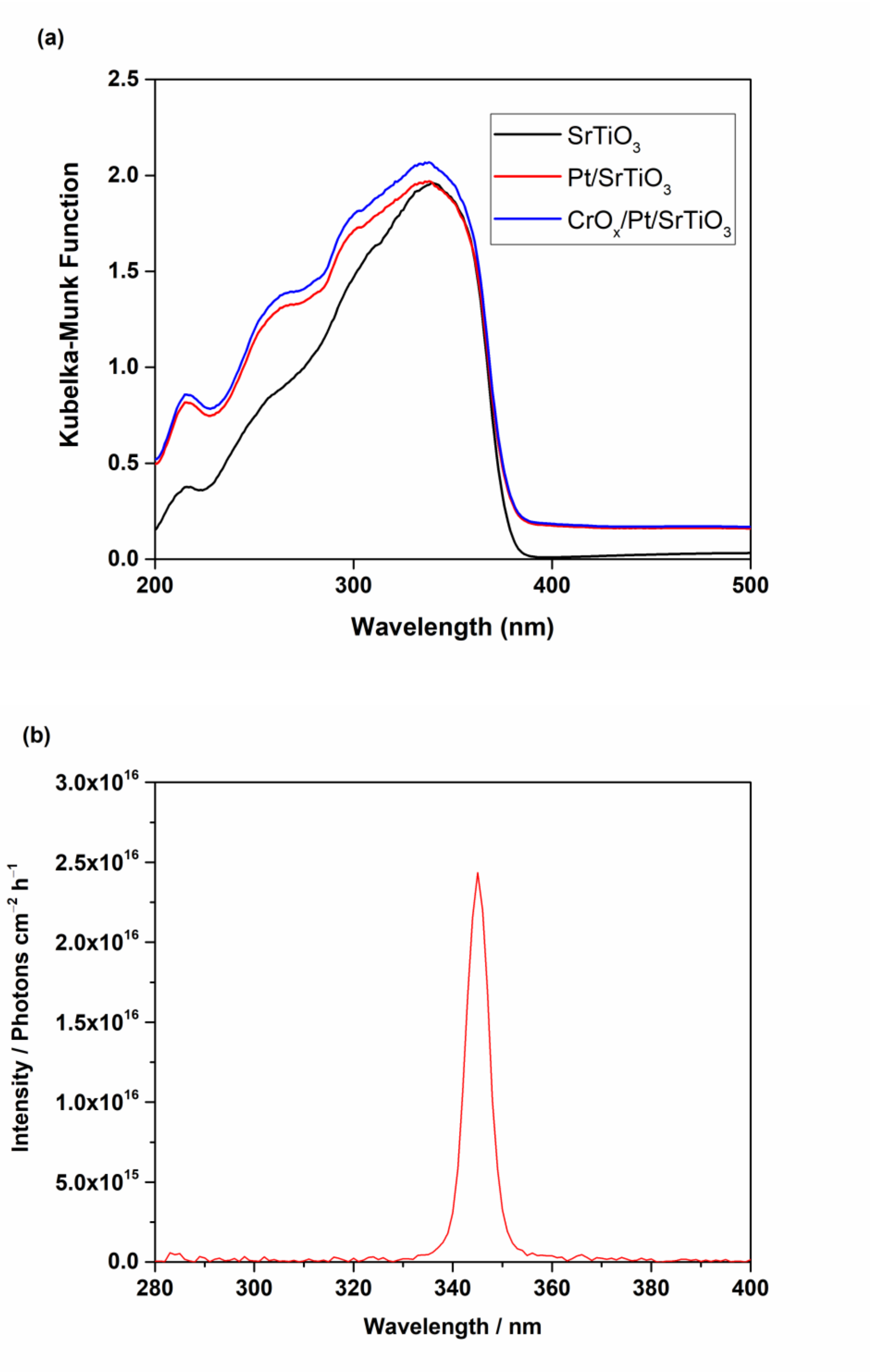

Figure S9. (a) Diffuse reflectance UV-Vis spectra of bare flux-treated SrTiO$_3$, Pt/SrTiO$_3$, and CrOx/Pt/SrTiO$_3$. (b) Photon flux of a UV-Vis lamp with a bandpass filter 35 (BP 35).

Potential breakdown for flat nanoscale electrolysis

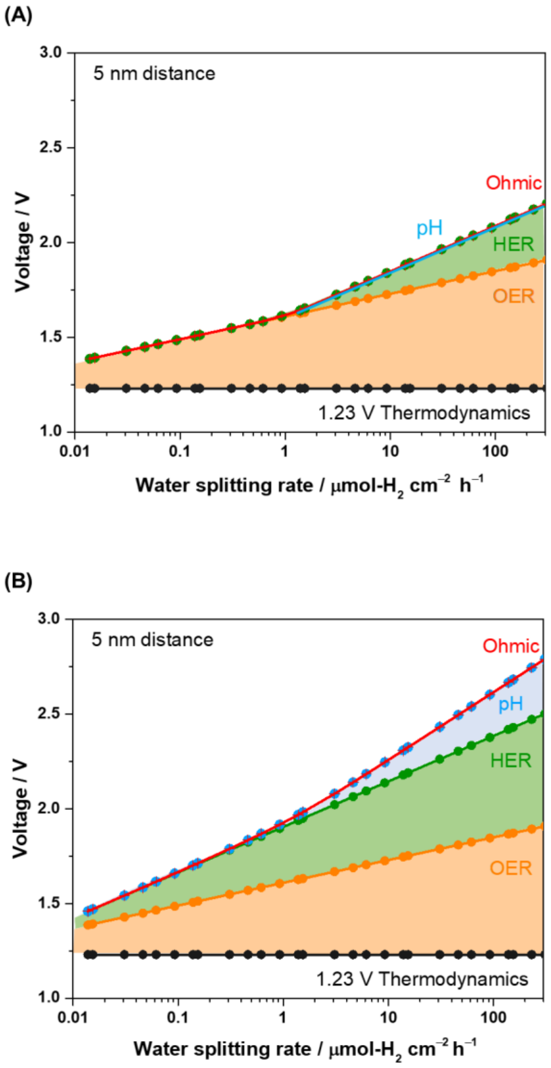

Figure S10. Nanoscale electrolysis PNP simulations of the relative potential distribution as a function of the logarithm of the water splitting rate, in the ideal flat system assuming an inter-particle distance of 5 nm with (A) buffered and (B) unbuffered electrolytes. The HER exchange current densities of (A) 3 mA cm^{-2} and (B) 1×10^{-2} mA cm^{-2} derived from Figure S8 were used. The potentials required for water splitting were separately analyzed according to the kinetics, mass transport contributions, ohmic drop, and Nernstian potential loss due to pH gradients.

The overpotentials originating from the kinetics, ohmic effects and Nernstian losses associated with pH gradients are shown in Figure S10A and S10B for buffered and unbuffered conditions, respectively, when the anodic and cathodic sites are 5 nm apart on the flat two-dimensional electrochemical device. Please note that this analysis is not representative of photocatalytic scenario because the band positions are not considered; e.g., the valence band edge of $SrTiO_3$ is over 1 V more positive than the OER equilibrium potential.[9] In general, the simulation results indicate that the ohmic drop is negligible under both buffered and unbuffered conditions at all water splitting rates, as previously discussed (Figure 3 of main manuscript). Under unbuffered conditions, the Nernstian potential losses from pH gradients appear to contribute only at rates starting from 1 μmol-H_2 cm^{-2} h^{-1}. Notably, Figure S10B shows significant HER overpotential even at low rates under unbuffered conditions due to the demanding kinetics for the reduction of water molecules. The calculations show that the HER kinetic overpotential required to achieve 10% STH efficiency (≈153 μmol-H_2 cm^{-2} h^{-1}) is approximately 500 mV under unbuffered conditions, as demonstrated in Figure 7 of the main manuscript, which is similar to the overpotential of OER. In contrast, the HER overpotential under buffered conditions is only large at water splitting rates greater than 10 μmol-H_2 cm^{-2} h^{-1}. The simulations show that the use of buffer decreases the HER overpotential by as much as 300 mV at 10% STH efficiency as a consequence of proton reduction achieved by the presence of buffering ions. In order to accurately describe the photocatalytic system, three-dimensional model instead of the flat-surface model is effective to reduce kinetic contribution by having more active sites, and additional overpotential losses must be accounted for including, but not limited to, carrier recombinations and interfacial losses.

One-dimensional theoretical descriptions

Conventionally, Fick's law theoretically describes diffusion:

$$J = -D\frac{\partial C}{\partial x}, \tag{S2}$$

where J is the diffusion flux, D is the diffusion coefficient, C is the concentration of the species of interest, and x is the distance. For Nernst-type diffusion, this equation is simplified into the following formula:

$$J = -D\frac{C_0}{\delta}, \tag{S3}$$

in which C_0 is the concentration of species in the bulk of the electrolyte and δ dictates the thickness of the diffusion layer. Importantly, for a spherical electrode, the thickness of the diffusion layer theoretically equals the radius of the electrode.[3]

As an initial attempt to apply the simple and well-established theory described above, a simulation of the diffusion flux in an electrocatalytic system (half-cell reaction) is developed herein. As a simplified starting model, a primitive packing of spherical electrodes with radius r on a flat surface is described below. In this system, eqn. S2 directly applies to the description of the diffusion flux for each particle, and therefore, the current density per particle j is expressed by

$$j = nFD\frac{C_0}{r}, \tag{S4}$$

where n is the number of electrons involved and F is the Faraday constant. Since the surface area of each hemispherical particle is expressed by $2\pi r^2$, the electric current per particle is given by

$$i = 2\pi nFDC_0 r\,. \tag{S5}$$

When this particle is periodically placed with an inter-particle distance of 2r on a substrate (square shaped, $A \times A$), the number of particles is simply described by $\left(\frac{A}{4r}\right)^2$. Therefore, the overall current is dictated by

$$i_{tot} = \frac{\pi nFA^2DC_0}{8r}, \tag{S6}$$

and the overall current density normalized by the geometric surface area of the substrate (A^2) is

$$j_{tot} = \frac{\pi nFDC_0}{8r}. \tag{S7}$$

In Figure S11a, the limiting diffusion current density for each particle and the substrate is plotted as a function of the particle size for the case of hydronium ion reduction at pH 5. The values shown indicate that in this simple model, when the total geometric current density is ca. 10 mA cm^{-2} (at a particle size of 70 nm), the local current density for each particle can be as high as 26 mA cm^{-2}.

To obtain further insights into conditions relevant to practical systems, the following conditions are considered: 40 wt.% Pt loaded on carbon (200 m^2 g^{-1}) placed on a flat substrate (1.5 mm diameter) with a loading of 35 μg$_{\mathrm{Pt}}$ cm^{-2}. The calculation results of this model are shown in Figure S11b. According to this figure, when the particle size of Pt is as small as several nanometers, the local current density per particle can be as high as 900 mA cm^{-2} with an overall geometric current density of 10^4 mA cm^{-2}. However, when this value is compared with those from experimental studies, such high limiting diffusion current densities cannot be obtained in practice.

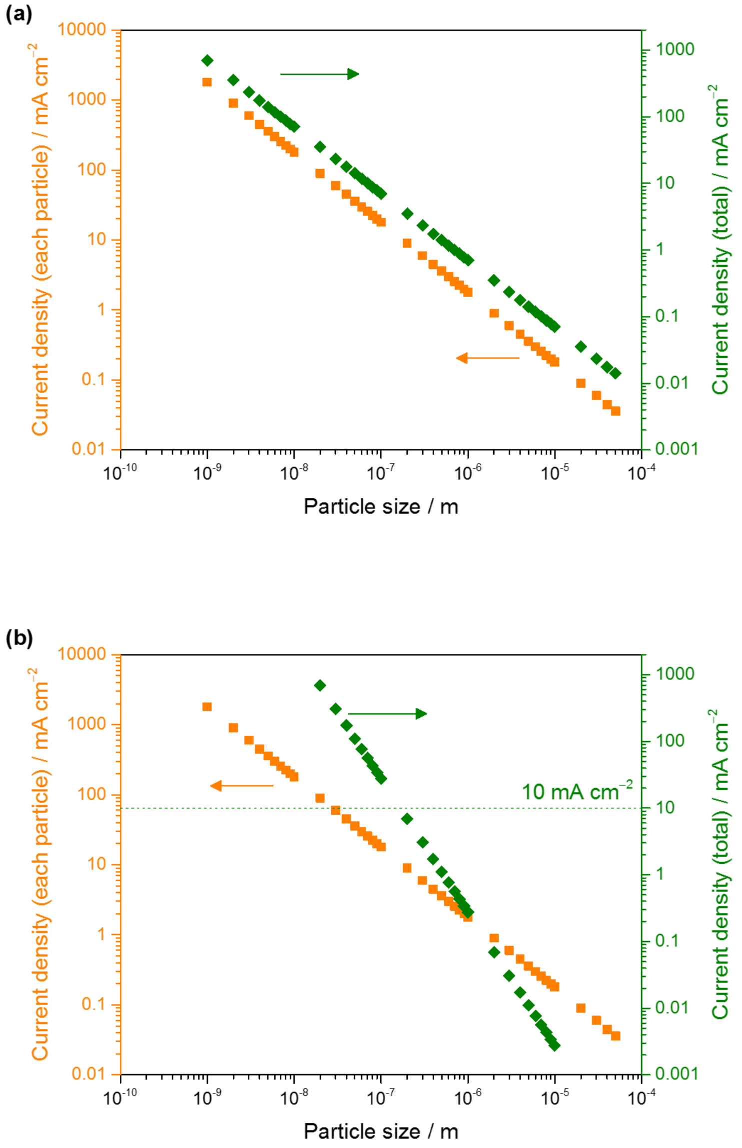

Figure S11. Simulated limiting diffusion current density for hemispherical particulate electrodes dispersed on a flat substrate for the reduction of hydronium ions at pH 5. The limiting diffusion current densities for both each particle and the substrate are shown as a function of the particle size. (a) Ideal system and (b) with a boundary condition of 40 wt.% Pt loaded on a carbon (200 m^2 g^{-1}) catalyst placed on a flat substrate (1.5 mm diameter) with a loading of 35 μgPt cm^{-2}.

To quantitatively elucidate the discrepancy, a revised model is considered: the radius of particle is fixed to 2 nm, and the thickness of diffusion layer is considered variable. In Figure S12a, the limiting current densities for each particle and the substrate are compiled as a function of the diffusion layer thickness. This simple calculation revealed that for such systems to provide the experimentally observed limiting diffusion current density (~10 mA cm^{-2}) in the RDE configuration, the thickness of diffusion layer needs to be approximately 10 to 20 μm.

Notably, in the RDE, the thickness of the diffusion layer is controlled by the disk-rotation speed. By comparing Fick's first law (eqn. S3) with the theoretical Levich equation[3]

$$j = 0.62nFD^{2/3}\omega^{1/2}\nu^{-1/6}C_0\,, \tag{S8}$$

in which ν is the kinematic viscosity and ω is the disk-rotation speed, the diffusion layer thickness is given as a function of the disk-rotation speed as follows:

$$\delta = 1.62D^{1/3}\nu^{1/6}\omega^{-1/2}\,. \tag{S9}$$

With this equation, the theoretical diffusion layer thickness is readily calculated and is compiled against the disk-rotation speed in Figure S12b.

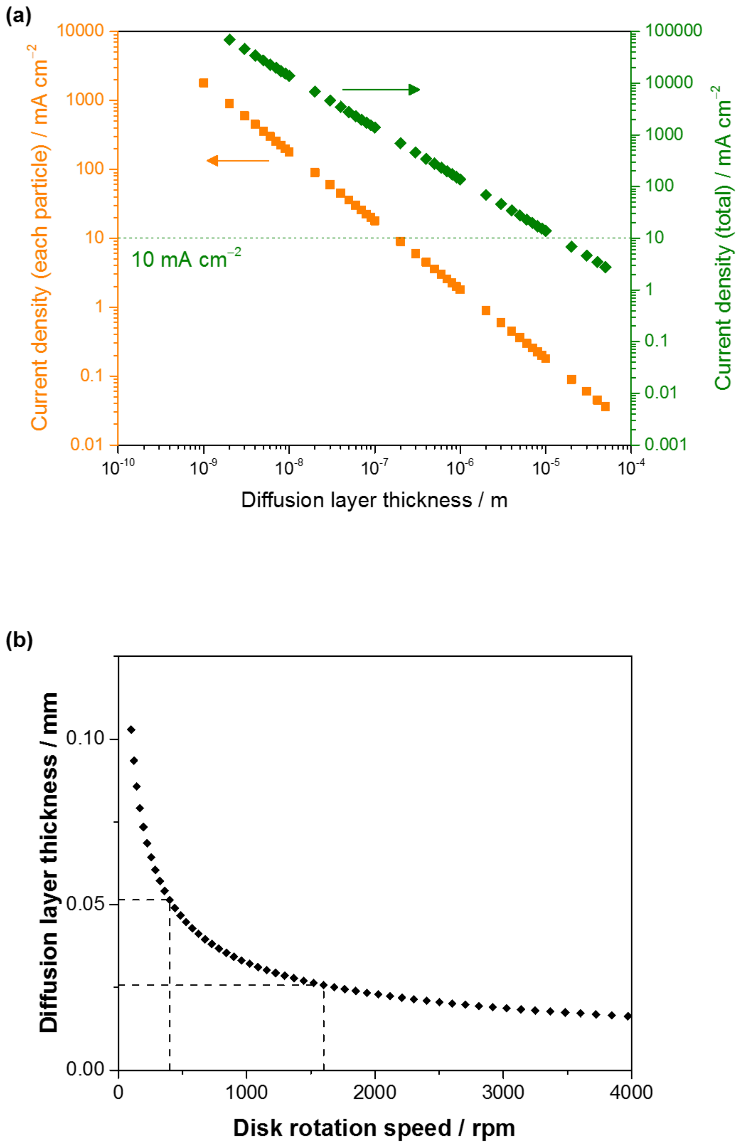

Figure S12. (a) Simulated limiting diffusion current density for hemispherical particulate electrodes dispersed on a substrate for the reduction of hydronium ions at pH 5 with a boundary condition of 40 wt.% Pt (Pt particle diameter of 4 nm) loaded on a carbon (200 m^2 g^{-1}) catalyst placed on a flat substrate (1.5 mm diameter) with a loading of 35 μg$_{Pt}$ cm^{-2}. (b) The thickness of the diffusion layer as a function of disk-rotation speed in the RDE configuration.

As shown in Figure S12b, in the typical RDE configuration, the planar diffusion is described by a diffusion layer thickness of several µm (e.g., 50 µm at 400 rpm and 17 µm at 1600 rpm), which is in quantitatively in good agreement with the observation in Figure S12a. Therefore, it can be concluded that even if nanosized particles are utilized on a macroscale RDE configuration, the diffusion flux is dictated by the planar diffusion. Notably, in such circumstances, pH values lower than 1.6 and higher than 12.4 are required to reach a limiting diffusion current density of 10 mA cm^{-2} for the hydronium ion reduction and hydroxide ion oxidation reactions, respectively, as shown in Figure S7. This situation would become apparent when the diffusion flux in planar flow is smaller than the overall diffusion flux of particulate electrodes. In other words, the diffusion layer for the particulate electrode would overlap in the practical system, resulting in the bulky diffusion layer covering all the substrate-liquid interface.

The discussion herein suggests that when forced convection is present and/or the nanosized electrocatalysts are located close to each other, mass transport events can be described by the planar diffusion model. Notably, the situation is more complicated when both reduction and oxidation sites are present on the same surface in mesoscopic dimensions, i.e., the photocatalytic system. Furthermore, the commonly utilized assumption of electroneutrality may not hold at such length scales in pure water (i.e., tenths to a hundred nanometers). In an attempt to elucidate the mass transport events in such conditions without convection, two-dimensional numerical experiments solving the Poisson-Nernst-Planck (PNP) equations were performed via finite element analysis as described in the main text and in Figure S4 utilizing the parameters described in Table S1.

Discussion of the extrapolation of the apparent quantum efficiency (AQE)

The calculation of the extrapolated apparent quantum efficiency (AQE) is elaborated herein. To calculate the AQE, a 350-nm bandpass filter was used to select a specific wavelength as shown in Figure S9c, and the photons were integrated in 300-400 nm. The photon flux was measured using an AvaSpec-3648 spectrometer, an AvaLight DHS calibration light source, and an FC-UV200-2 fiber-optic cable. The multiple measurements allowed integration of the total photon flux into the spectral area of the photocatalytic reactor (38.5 cm^2).[10] Using a bandpass filter reduced the incoming light intensity by ~99% at the cost of obtaining a clean distribution of photons at the specified wavelength (see Figure S9c). At such low light intensity, the unbuffered and buffered conditions provided the same rate, as observed in Figure 9a from the main text. However, once the filter was removed and a higher light intensity passed into the reactor, a clear difference in the H_2 evolution rate was observed between the two solutions. The AQE was calculated as shown below in eqn. S10.

$$\mathrm{AQE}(\%) = \frac{\text{The rate of } \mathrm{H_2} \text{ evolution} \times 2}{I(\lambda)} \times 100 \qquad \text{(S10)}$$

where $I(\lambda)$ is the photon flux at a specific wavelength. The AQE was first calculated for unbuffered conditions, and the rest of the data were proportionally extrapolated to the measured H_2 evolution rate under each condition.

References

1. N. M. Marković, T. J. Schmidt, V. Stamenković, P. N. Ross, *Fuel Cells.*, 2001, **1**, 105-116.
2. T. Shinagawa, K. Takanabe, *Phys. Chem. Chem. Phys*., 2015, **17**, 15111-15114.
3. A. J. Bard, L. R. Faulkner, *Electrochemical Methods Fundamentals and Applications*; Wiley: New York, 2001.
4. T. Shinagawa, K. Takanabe, *J. Phys. Chem. C*, 2015, **119**, 20453-20458.
5. T. Shinagawa, K. Takanabe, *ChemSusChem*, 2017, **10**, 1318-1336.
6. T. Shinagawa, K. Takanabe, *J. Phys. Chem. C*, 2016, **120**, 1785-1794.
7. W. Kunz, *Specific Ion Effects,* World Scientific Publishing Co. Pte. Ltd., Singapore, 2010.
8. T. Shinagawa, M. T.-K. Ng, K. Takanabe, *ChemSusChem*, 2017, **10**, 4155-4162.
9. M. M. Waegele, X. Chen, D. M. Herlihy, T. Cuk, *J. Am. Chem. Soc.*, 2014, **136**, 10632-10639.
10. M. Qureshi, K. Takanabe, *Chem. Mater.*, 2017, **29**, 158-167.